Modeling Structural Morphology of Microporous Carbons by Reverse Monte Carlo

Kendall T. Thomson* and Keith E. Gubbins

Department of Chemical Engineering, North Carolina State University, Raleigh, North Carolina 27695

We present a realistic model of carbon pore morphologies based on molecular simulation. Reverse Monte Carlo (RMC) techniques are used to generate model carbon structures composed of rigid carbon basal plates. Arrangement of the carbon plates is driven by a systematic refinement of simulated carbon–carbon radial distribution functions to match experiment. The RMC procedure was first tested by comparing a model output structure to a hypothetical input structure generated through molecular dynamics techniques. Structural characteristics of the RMC model such as porosity, surface area, pore-size distribution, and surface-averaged energy distributions were in close agreement with those for the input structure, thus validating the RMC method. We also studied the structural characteristics of a model output generated from a real, activated mesocarbon microbead (a-MCMB). The porosity, surface area, and simulated N_2 isotherm are compared with experiment. Nitrogen adsorption isotherms for our model carbon structures, generated by grand canonical MC techniques, show a pore morphology that is generally non-slit-like and highly connected with evidence of localized capillary condensation occurring in regions with pores of around 14.5 Å and higher.

1. Introduction

Activated carbons have long been used as industrial sorbents for a wide variety of commercial applications. Originally used for sugar purification,[1] the potential of activated carbons has since been recognized and applied to such commercial uses as drinking water purification,[2] solvent recovery,[3] deodorization,[4] and air purification.[5,6] Furthermore, activated carbons have been used extensively as catalyst support in chemical processing applications.[7–11]

The widespread interest and applicability of activated carbons as adsorbents derives from their high adsorption capacity. This, and the fact that carbonaceous materials are relatively cheap to produce, makes activated carbons an important class of materials. Key to understanding and ultimately predicting adsorption phenomena is the determination of the true nature of microporosity within these structures. Subsequently, a great deal of interest exists in characterizing the pore structure of activated carbons.

Porous carbons in general are recognized as defective derivatives of crystalline graphite.[12] Graphite consists of polyatomic, aromatic carbon sheets (sp^2 hybrid bonding) layered atop one another in a hexagonal close packed arrangement (i.e., alternating layers in a hexagon unit cell).[13] The fully crystalline structure yields an interlayer spacing of 3.35 Å. Porous carbons, such as activated carbons, carbon fibers, carbon blacks, and vitreous carbons, are often thought of as disordered arrangements of defective crystallites of graphite.[14] Depending on the degree of graphitizibility (i.e., the ability for a given carbon material to transform to graphite under severe heat treatment), the size and shape of graphite crystallites are known to vary. Domains of orientational order, where microcrystallites tend to more or less align in similar directions, are also observed.[15]

The more easily graphitizing carbons (i.e., "hard" carbons) tend to have less defective, larger crystallites—characterized by a higher abundance of aromatic rings per plate. They are observed to possess large domains of orientational order (i.e., mesoscale order). Such "hard" carbons are weak adsorbents due to a relatively low degree of, and accessibility to, microporosity. On the other hand, nongraphitizing carbons such as activated carbons exhibit a much more open structure characteristic of highly defective carbon plates and subsequently smaller regions of orientational order (microscale order). Activated carbons show a greatly enhanced degree of microporosity compared to "hard" carbons. Further these micropores are presumed, due the much lower densities typical of activated carbons, to be highly accessible.

Activated carbons are produced commercially from a wide variety of carbon-based raw materials including coal, wood, peat, coconut shell, lignite, and certain petroleum byproducts such as pitch.[16] These raw materials are converted to porous carbon through a two-stage process of *carbonization* and *activation*.[17] Carbonization consists

(1) Smisek, M.; Cerny, R. S. *Active Carbon*; Elsevier: Amsterdam, 1970.
(2) Hyndshaw, A. Y. *J. New Engl. Water Works Assoc.* **1965**, *79*, 236.
(3) Rowe, R. N. *Air Eng.* **1964**, *6*, 15.
(4) McDowell, L. *J. Appl. Polym. Sci.* **1961**, *5*, 663.
(5) Kahle, H. *Chem. Ing. Tech.* **1953**, *25*, 144.
(6) Kahle, H. *Chem. Ing. Tech.* **1954**, *26*, 75.
(7) Trapnell, B. M. W. In *Catalysis*; Emmett, P. H., Ed.; Rheinhold Publ. Corp: New York, 1955; Vol. 3, p 1.
(8) Cheney, H. A.; McAllister, S. H.; Fountain, E. N.; Anderson, J.; Peterson, W. H. *Ind. Eng. Chem.* **1950**, *42*, 2580.
(9) Rodriques-Reinoso, F. *Carbon* **1998**, *36*, 159.
(10) Arumugam, B. K.; Wankat, P. C. *Adsorption* **1998**, *4*, 345.
(11) Nemati, M.; Webb, C. *J. Chem. Technol. Biot.* **1999**, *74*, 562.
(12) Oberlin, A. In *Chemistry and Physics of Carbon*; Marcel Dekker: New York, 1990; Vol. 22.

(13) Bernal, J. D. *Proc. R. Soc. London, Sect. A* **1924**, *106*, 749.
(14) McEnaney, B. *Carbon* **1988**, *26*, 267.
(15) March, H.; Walker, P. L., Jr. In *Chemistry and Physics of Carbon*; Marcel Dekker: New York, 1979; Vol. 15, Chapter 3.
(16) Wilson, J. *Fuel* **1981**, *60*, 823.
(17) Bansal, R. C.; Donnet, J.-B.; Stoeckli, F. In *Active Carbon*; Marcel Dekker: New York, 1976.
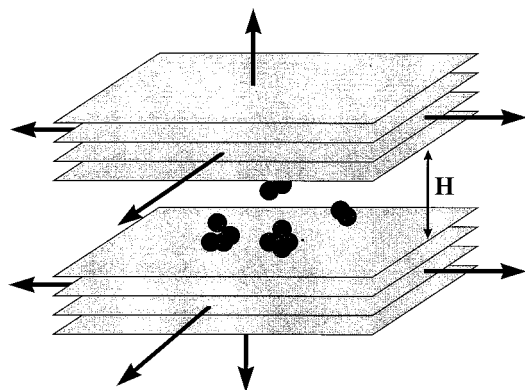
Figure 1. Schematic of the *slit-pore model* for adsorption in planar geometries.

of the thermal degradation of raw material first into a disorganized carbon residue, followed by condensation into organized polyaromatic sheets. In this stage, noncarbon-aceous volatiles are expelled from the structure leaving a preliminary framework of mostly carbon. However, depending on the nature of the raw material a significant concentration of non-carbon heteroelements, such as oxygen, sulfur, and hydrogen, can exist. Often, as in the case of oxygen, these heteroelements serve as bridging units to connect graphite-like sheets to one another. This results in framework cross-linking and accounts for further structural defects. Microporosity in these structures is greatly enhanced through the process of activation, whereby residual disorganized carbon is burned away through pyrolisis in a strongly oxidizing environment. The activation process additionally widens existing pores by pyrolizing existing aromatic carbon—in effect burning away smaller carbon sheets and creating holes and defects in larger sheets.

In characterizing micro- and mesoporosity in activated carbons, it is convenient to try and simplify the representation to some extent. The earliest and most common model used in simulation work is an idealization based on the above observations of porous carbon morphology. The *slit pore model* assumes that adsorbates sorb in pores that are planar in geometry and slitlike in topology. A standard carbon pore is represented as the space between two graphite-like layered crystallites aligned perfectly parallel and extending to infinity in all directions (Figure 1). The main parameter of this model is the separation distance (H) between the parallel plates—designated as the pore width. The advantage of such a simplistic model is that it is purely geometric and does not depend on the specifics of the carbon structure. This fact allows one to develop a completely theoretical description of adsorption and further explore the fundamentals of confined fluids behavior.

The slit pore model has had great success in developing the theoretical basis for adsorption in porous carbons, and a number of such studies have been made.[18–24] Perhaps the greatest utilization of the model is as a "basis set" for determining pore size distributions of real carbons from experimental adsorption isotherms. The experimental

isotherm of a carbon can be expanded as a linear combination of theoretical isotherms of differing pore sizes (H). Thus

$$\theta_{\exp}(P,T) = \int \theta_{\sim}(P,T,H)\, f(H)\, \mathrm{d}H \qquad (1)$$

where $\theta_{\exp}$ is the experimental isotherm and $\theta_{\sim}$ is the simulated isotherm in a slit pore of width H. The function $f(H)$ represents the pore size distribution function and can be determined from experiment by inverting the integral in (1).

Despite the slit pore model's success, it is based on the assumption of a fixed ideal pore morphology (smooth planer pores). It also assumes a limited ideal pore topology in which adsorbates in pores of differing widths do not interact. Further, the idealized topology does not take connectivity between pores into account. Nor does it allow for adsorption effects along crystallite boundary edges. In the "hard" graphizable carbons it is assumed these effects are minor since the large, relatively nondefective carbon planes account for the majority of the observed porosity. However it can be expected that the slit pore model offers a poor representation of activated carbons where deviations from nondefective crystallites are prominent.

Recently, several models have surfaced that try to account for the deficiencies of the slit pore model. McEnaney et al.[25] introduced an adjustable slit pore model that allowed for a variable number of carbon plates per crystallite. Also, instead of using graphite-like crystallites, McEnaney allowed the separation distance between plates within the crystallites to vary. This model could then be used in conjunction with experimental characterization data—in effect incorporating plate separation, average crystallite size, and carbon density. The model put forth by McEnaney does account for energetic effects due to non-graphite-like crystallites; however, it does not address the true pore topology and morphology of the pores. Rodriguez et al.[26] went a long way in accounting for pore topology by introducing a model composed of individual carbon sheets of finite size. These sheets are arranged in parallel (yet offset) configurations and linked to one another through oxygen bridges. Through a relatively few number of parameters, deviations in slitlike pore topologies could be generated that offer some degree of connectivity approaching that of the true carbon structure.

Segarra and Glandt[27] developed a model of activated carbon that attempted to capture the long-range pore topology yet still hold to the slit pore idealism. On the basis of a model conceived by Eppenga and Frenkel,[28] they developed a carbon structure composed of platelets of graphite-like crystallites arranged isotropically in a periodic simulation cell. Monte Carlo moves were then used to develop a disordered arrangement of platelets in some random configuration. A similar model was proposed by Dahn et al.,[29] termed the *falling cards model*. Like Segarra and Glandt's model, ideal carbon plates were arranged with a disordered packing through a procedure that mimics cards falling on top each other. Both models generated structural heterogeneity not explicitly present in the slit pore model.

Another modification of the slit pore model is the "randomly etched graphite" (REG) model of Seaton et al.[30]

(18) Nicholson, D. *J. Chem. Soc., Faraday Trans.* **1996**, *92*, 1.
(19) Tan, Z; Gubbins, K. E. *J. Phys. Chem.* **1992**, *96*, 845.
(20) Jiang, S.; Zollweg, J. A.; Gubbins, K. E. *J. Phys. Chem.* **1994**, *98*, 5709.
(21) Shigeta, T.; Yoneya, J.; Nitta, T. *Mol. Simul.* **1996**, *16*, 291.
(22) Gusev, V. Y.; O'Brien, J. A. *Langmuir* **1998**, *14*, 6328.
(23) Nguyen, C.; Do, D. D. *Langmuir* **1999**, *15*, 3608.
(24) Lastoskie, C.; Gubbins, K. E.; Quirke, N. *J. Phys. Chem.* **1993**, *97*, 4786.

(25) McEnaney, B.; Mays, T. J.; Chen, X. *Fuel* **1998**, *77*, 557.
(26) Rodriguez, J.; Ruette, F.; Laine, J. *Carbon* **1994**, *32*, 1536.
(27) Segarra, E. I.; Glandt, E. D. *Chem. Eng. Sci.* **1994**, *49*, 2953.
(28) Eppenga, R; Frenkel, D. *Mol. Phys.* **1984**, *52*, 1303.
(29) Dahn, J. R.; Xing, W.; Gao, Y. *Carbon* **1997**, *35*, 825.
(30) Seaton, N. A.; Friedman, S. P.; MacElroy, J. M. D.; Murphy, B. J. *Langmuir* **1997**, *13*, 1199.

This model begins with a conventional slit pore consisting of parallel pore walls—two graphite layers deep. However, carbon atoms are randomly removed from the innermost graphite planes, producing structural heterogeneity along the pore walls, yet still perserving the slit pore geometry. The surface roughness provided by the REG model represents a more realistic pore boundary than the smooth walls assumed in the slit pore model. As a result, diffusion coefficients measured using the REG model are much closer to experimental values. Other models have been proposed to account for surface heterogeneity on graphite plates. Bojan and Steele[31] present a model based on stacking truncated graphite basal planes of fixed size to produce a stepped surface. Riccardo et al.[32] proposed a simple model in which one distributes adsorption energies over a lattice of surface sites. The manner in which the energies are distributed is based on an arbitrary distribution function that can incorporate nonlocal spacial correlations as desired.

While all of the above models do incorporate deviations from the ideal slit pore model, they still fall short of representing the true carbon structure. What is needed is a model that systematically incorporates a reasonable representation of (1) the true carbon morphology, (2) the true pore morphology, and (3) the true pore topology, yet can be used with reasonable efficiency in modern simulation studies. We define *pore morphology* as the geometric shape and structure of the pore from both a pore volume and pore surface perspective—i.e., pore volume characterized as slitlike versus cylindrical, and surface features characterized as smooth versus corrugated or rumpled. We define *pore topology* as a description of the pore arrangement relative to other pores. We use pore topology to specify the connectivity of pores and describe the macroscopic environment seen by adsorbed fluids within the carbon structure.

To achieve an accurate description of these characteristics, models should also rely extensively on experimental characterization as input. We propose here a model that accomplishes this through molecular simulation. Our model uses a reverse Monte Carlo (RMC) algorithm that allows us to build a representation of a real carbon structure through successive refinement of experimental correlation functions such as the carbon—carbon radial distribution function (RDF) and tunneling electron microscopy (TEM) micrograph data. The size of the resulting carbon representation (i.e., simulation cell) can be chosen appropriately to accomplish whatever fundamental study is desired.

The rest of the paper is arranged as follows. Following this introduction, we introduce in section 2 the RMC methodology and lay out the details of our carbon model. We define the basic structural units and give details on the method for generating a carbon representation from experimental RDFs. In section 3 we test the validity of our method by first generating a simulated carbon structure (referred to hereafter as [TARGET]) using molecular dynamics simulations, to be used as a hypothetical experimental structure. We then use our model to generate an output structure (hereafter referred to as [MODEL]) and systematically compare the structural features of these two carbons. In section 4 we introduce various characterization techniques relevant to the model representation, including porosity, surface area, pore size distribution, and surface heterogeneity measures. We then use these techniques to further analyze and compare the structures [TARGET] and [MODEL]. In section 5 we present results from grand canonical Monte Carlo simulations of nitrogen adsorption in our model carbon [MODEL]. We show that the structural features of our model identify discrepancies in the slit pore characterization of micropores. In section 6 we present results for a model constructed from an experimental carbon—an activated mesocarbon microbead [a-MCMB]. We compare structural properties such as density, porosity, surface area, as well as nitrogen isotherm data. Finally in section 7 we discuss the ramifications of our work and suggest new directions of study in molecular simulations of carbons.

2. Model Details

There are several examples in the literature of what has become known as the reverse Monte Carlo (RMC) method.[33-35] Originally proposed by McGreevy and Putszai,[33] the method has recently been applied to atomic structure determinations of amorphous hydrogenated carbons.[36-38] The idea mirrors that of traditional Monte Carlo methods in which some initial atomic configuration is systematically changed through a well-defined stochastic procedure. The main difference is in the acceptance criteria applied for moves. Rather than basing acceptance on ensemble probability functions, as in the Metropolis algorithm,[39] moves are accepted in the RMC method based on whether they improve simulated correlation functions compared to experimental inputs.

The correlation functions of interest in our model are the carbon—carbon and adsorbate—adsorbate radial distribution functions, and void—void correlation functions generated from TEM micrographs. Experimental RDFs can be obtained from small-angle X-ray scattering (SAXS) and neutron scattering (SANS) by Fourier transform of the structure factor $S(q)$ via[40]

$$4\pi r^2 \rho(g(r) - 1) = \frac{2}{\pi} \int_0^\infty qr(S(q) - 1) \sin qr \, dq \quad (2)$$

where q is the magnitude of the elastic scattering vector

$$q = \frac{4\pi}{\lambda} \sin \frac{\theta}{2} \quad (3)$$

λ is the incident wavelength, and θ is the scattering angle. The RDF $g(r)$ represents the probability of finding a scatterer at a distance r away from another scatterer and can be directly calculated in simulations. The structure factor $S(q)$ is related to the scattered beam intensity, corrected, and normalized appropriately. If one has an accurate measure of ρ, the average number density of scatterers, then the RDF can be directly determined from experiment.

We begin by generating an initial carbon structure within a three-dimensional, cubic simulation cell with periodic boundary conditions. The basic carbon units of

(31) Bojan, M. J.; Steele, W. A. *Langmuir* **1993**, *9*, 2569.
(32) Riccardo, J. L.; Steele, W. A.; Ramirez Cuesta, A. J.; Zgrablich, G. *Langmuir* **1997**, *13*, 1064.

(33) McGreevy, R. L.; Putszai, L. *Mol. Simul.* **1988**, *1*, 359.
(34) McGreevy, R. L.; Howe, M. A.; Keen, D. A.; Clausen, K. *IOP Conf. Ser.* **1990**, *107*, 165.
(35) da Silva, F. L. B.; Svensson, B.; Akesson, T.; Jonsson, B. *J. Chem. Phys.* **1998**, *109*, 2624.
(36) McGreevy, R. L.; Howe, M. A.; Nield, V. M.; Wicks, J. D.; Keen, D. A. *Physica B* **1992**, *180 & 181*, 801.
(37) Walters, J. K.; Rigden, J. S.; Newport, R. J. *Phys. Scr.* **1995**, *T57*, 137.
(38) Rigden, J. S.; Newport, R. J. *J. Electrochem. Soc.* **1996**, *143*, 292.
(39) Metropolis, N.; Ulam, S. *J. Am. Stat. Assoc.* **1949**, *44*, 335.
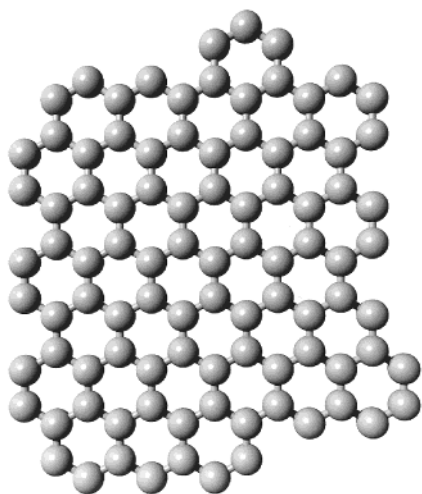(40) Warren, B. E. *X-ray Diffraction*; Dover Publications: New York, 1990; p 116.

Figure 2. Atomistic representation of a typical carbon plate unit used in our RMC simulation method.

our model consist of rigid, aromatic sheets of sp^2 bonded carbon. The diameters of the carbon atoms were taken to be 1.42 Å, and the interatomic distance used for the carbon atoms was that of graphite (1.42 Å). Starting with a target value of the carbon number density ρ_t, we construct carbon plates by randomly adding aromatic rings to the exposed edges of a starting ring. As the plates are generated, exposed edges have equal likelihood of receiving the next ring. The total number of aromatic rings for a given plate are determined by sampling from a Gaussian distribution of plate sizes. The average number of rings ($\bar{n}_r$), and the standard deviation (σ_r) are model inputs and represent guesses for the carbon structure of interest. Plates are systematically generated until the total density matches the target density ρ_t. Figure 2 shows what a typical carbon plate would look like. These plates are randomly placed in the simulation cell, roughly aligned along the same direction but with random deviations in their angles of tilt.

Simulated values of $g(r)$ are calculated by first discretizing the interatomic separation r into equal-sized bins. Next we generate a histogram of the number density of carbon atoms separated from each atom by a distance r. The RDF is then calculated by averaging this distribution over all carbon atoms in the structure. Since our model structure is composed of rigid carbon plates, we must impose artificial broadening of those peaks due to *intraplate* contributions. We accomplished this by splitting $g(r)$ into *intraplate* and *interplate* contributions. Simple Gaussian broadening of the *intraplate* $g(r)$ is imposed, and the two contributions are added to acquire the simulated RDF.

The Monte Carlo moves fall into three categories, (1) configurational moves, (2) ring creation/annihilation, and (3) plate creation/annihilation. The configurational moves include both translation and reorientation of the carbon plates (referenced by their centers of mass). Following the Metropolis procedure, we randomly select a carbon plate and then allow a 50/50% probability of either translation or reorientation. We store the RDF calculated before the move $g_{old}(r)$ and generate a new RDF after the move $g_{new}(r)$. Both of these functions are compared to the experimental distribution function $g_{exp}(r)$ obtained from eq 2 above by constructing the square deviation

$$\chi^2 = \sum_{i=1}^{n} (g(r_i) - g_{exp}(r_i))^2 \qquad (4)$$

Here the summation is over discretized values of r, the interatomic separation. The move is accepted only if the square deviation after the move is smaller that before the move, i.e., $\chi_{new}^2 < \chi_{old}^2$.

For the ring creation/annihilation moves we again randomly select a plate and allow a 50/50% probability of either creating or annihilating a ring from the boundary of the plate. Each boundary ring has an equal probability of being selected during annihilation moves, and each exposed edge is equally likely to accept a ring during creation. Equation 4 is used to calculate mean square deviations for the radial distribution functions before and after the move, and the same acceptance criterion is used.

The ring creation/annihilation moves provide a source and sink of carbon atoms in the simulation cell. As the carbon plate sizes adjust to the experimental distribution functions, the total carbon density may deviate substantially from the target density. This would occur if the initial guess for the average number of rings per plate was inaccurate. To provide a mechanism for maintaining the desired carbon density, we periodically allow plate creation or annihilation moves. For plate annihilation, we randomly select a carbon plate for destruction with equal probability. The same acceptance criterion described above is used. For creation, we randomly select a carbon plate and then generate an exact duplicate plate. This new plate is randomly inserted into the simulation cell and acceptance is based on the usual criterion. Plate creation/annihilation moves are only used when the simulated density deviates from the target value by some prescribed amount (1−5% depending on the desired accuracy of the final carbon density). If the carbon density deviates above the target value, then plate annihilation is introduced. Likewise for plate creation if the density deviates below the target.

During the RMC run, we alternate between configurational moves and ring creation/annihilation moves. A typical cycle would contain 100 translations and reorientations followed by 100 ring creation/annihilation moves. Plate creation/annihilation moves are included in the ring moves if necessary. Cycles continue until the mean square deviation function is determined to be converged and oscillating about some residual value.

3. Simulated Carbon Structures

To test our model and the RMC method, we have conducted a sample trial by generating a model carbon (using RMC) from a hypothetical carbon. The hypothetical carbon (hereafter referred to as [TARGET]) was actually generated through simulation; however, it served as the "experimental carbon" and thus as input for the RMC procedure. By using a hypothetical carbon structure, we have at our disposal the *exact* atomic configuration, which is to be compared with our RMC model carbon. This analysis therefore serves as a diagnostic check of our procedure by providing direct comparisons between input and output structures.

We created our carbon [TARGET] through a molecular dynamics simulation. We began with an initial carbon structure generated in the exact manner described in section 2. We used as our model inputs the values of $\rho_t = 1.138$ g/cm^3, $\bar{n}_r = 35$, and $\sigma_r = 10$. A periodic simulation cell measuring 50 Å on a side was used. From this initial configuration we used canonical molecular dynamics[41] to equilibrate the structure at 300 K. The plates were held rigid, and a Lennard-Jones interaction potential was used to represent forces and interaction energies between carbon atoms of differing plates. Values of $\sigma_{CC} = 3.40$ Å

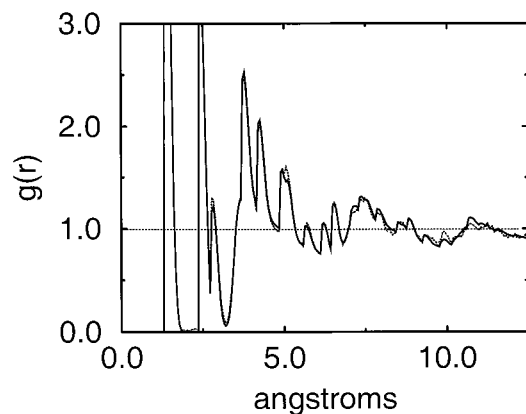(41) Nose, S. *Mol. Phys.* **1984**, *52*, 255.

Figure 3. C−C radial distribution function for the [TARGET] structure (solid line) and the converged [MODEL] structure (gray dotted line).
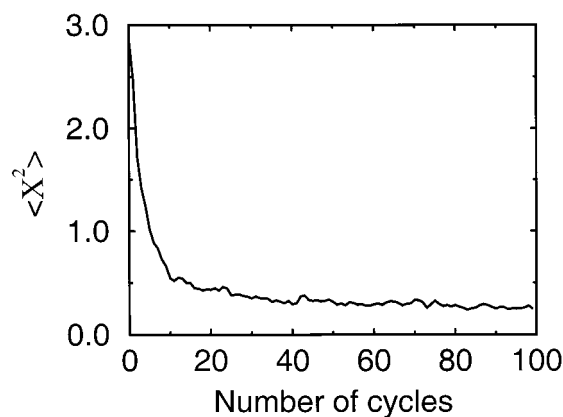

Figure 4. Convergence of the square deviation function χ^2 as a function of RMC simulation cycles for the generation of the [MODEL] structure. Here one cycle consists of 100 configurational moves plus 100 ring creation/annihilation moves.

and ϵ_{CC} = 28 K were used for the Lennard-Jones parameters.[42] After the carbon structure had equilibrated, we began a collection run of 200 ps at 300 K in which we sampled and averaged the carbon−carbon RDF. This function was then used as the target input function $g_{target}(r)$ (Figure 3), replacing the experimental function. We decided to use a time-averaged RDF at room temperature in order to provide a more realistic value of $g_{target}(r)$. This should provide a better test of our model as a representative static realization of an ensemble-averaged correlation function.

As our starting configuration for the RMC model, we choose a carbon structure generated with a different input density ($\rho = 1.10$ g/cm³). We also forced each carbon plate to have exactly 20 rings but allowed for random construction of the plates as per section 2. A simulation cell of 50 Å per side was used as with the hypothetical real carbon. RMC cycles containing 100 configurational moves and 100 ring creation/annihilation moves each were conducted, and the square deviation function χ^2 was carefully monitored until convergence was assured. The final output structure is hereafter referred to as [MODEL]. Figure 3 contains the converged RDF $g_{out}(r)$ for the carbon [MODEL] compared to the target function. We note that there is very little difference between the two functions with close to perfect overlap up to 13 Å. Figure 4 shows the convergence properties of the distribution functions
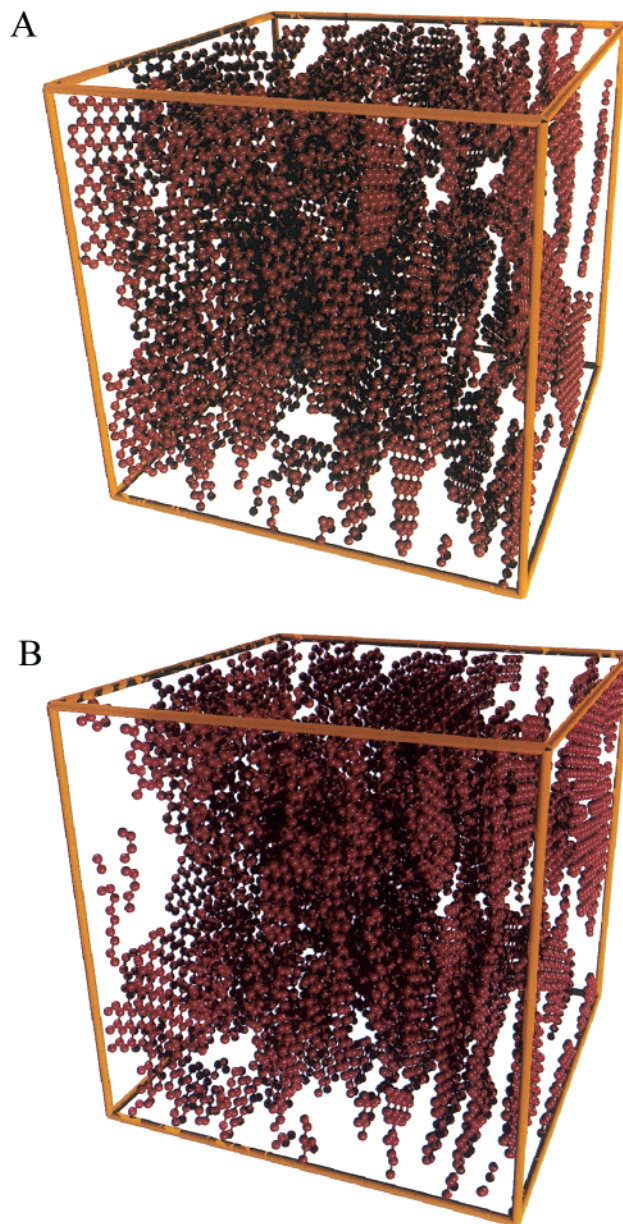
(42) Steele, W. A. *The Interaction of Gases with Solid Surfaces*; Pergamon Press: Oxford, 1974.

Figure 5. Structural representaion of (A, top) the structure [TARGET] and (B, bottom) the converged structure [MODEL]. Red spheres represent carbon atoms which are shown at a scale much less than their van der Waals radii for reasons of clarity.

through the course of the simulation. The entire RMC run comprised 100 cycles.

Figure 5 contains snapshots of both the [TARGET] structure (A) and the [MODEL] structure (B). The [TARGET] structure was obtained from the final atomic positions of the molecular dynamics collection run. Both structures show a similar alignment of plates along a preferred direction. Microcrystallites are present with typically two to three plates in a group. The minimum separation distance between plates was found to be approximately 4 Å (larger than the graphite separation of 3.38 Å) and agrees with experimental values for several real carbons. The most striking feature of the structures is the large portion of void space for which the slit-pore representation seems to be inaccurate. The morphology of pores in these regions is decidedly heterogeneous in that the pores are irregularly shaped and contain both planer surfaces and carbon plane edges as bounding

Table 1. Comparison of the Structural Properties of the [TARGET] Structure and the [MODEL] Structure

	target structure	simulated structure
density, g/cm^3	1.138	1.141
n_r (rings/plate)	34.68	34.05
σ_r (std dev)	0.95	7.78
carbons/plate	96.49	96.62
porosity	0.482	0.485
surface area, m^2/g	526	587

surfaces. For this particular carbon structure, most of the pore volume appears to be non-slitlike.

In Table 1 we present a comparison of the structural properties for the two carbon structures. Despite starting with an initial carbon density lower than that of our hypothetical target density, the final output density is within 0.3% of the target. We also see good argeement between [TARGET] and [MODEL] for porosity and surface area (see section 4). However, a comparison of the plate size distributions shows conflicting results. The average number of rings per plate in both structures varied by less than 2%. However the [MODEL] structure seemed to be more disperse having a standard deviation in ring number of 7.78 compared to 0.95 for the [TARGET] structure. It is possible that this discrepancy is due to the use of an ensemble averaged RDF for $g_{target}(r)$. Although $g_{target}(r)$ would represent the true mean value $\bar{n}_r$, thermal motion could account for the artificially high variance reflected in the [MODEL] structure. The reason is that the [MODEL] carbon RDF is calculated with a static carbon lattice whereas the [TARGET] carbon RDF is an ensemble-averaged function. The [TARGET] RDF therefore contains broadening due to thermal motion that cannot be directly realized in the model RDFs. Such a broadening could be accounted for artificially in the [MODEL] RDF through a broadened distribution of plate sizes. Since experimental distribution functions obtained from scattering experiments are by nature averaged quantities, it would appear that some caution should taken in interpreting plate size distributions obtained from our model.

4. Structural Characterization

Having developed a model that includes a detailed accounting of carbon atom positions, we now describe a series of characterization techniques that can be directly applied. Most of these methods derive from combinations of simple Monte Carlo integration techniques and procedures used in quantitative stereology. Some of these methods have been previously applied to models of controlled-pore glasses[43] and are presented here with modification where necessary.

4.1. Porosity. We define the porosity of a carbon structure as the fraction of total space available to some adsorbate. Such a definition is inherently dependent on the choice of adsorbate. For this work, all porosities reported are based on nitrogen adsorption properties assuming a spherical approximation for molecular nitrogen. The *spherical approximation* involves representing nitrogen as a single Lennard-Jones sphere and defining interaction parameters for N_2 with other N_2 molecules and with carbon atoms. The values of σ and ϵ used[42] in this study are presented in Table 2.

We must at this point clarify what we mean by "available space". We can envision placing adsorbate molecules randomly into our structure and measuring the closest distance to any carbon atom on the lattice. If this distance is less than some cutoff value, then the insertion is not allowed. A reasonable choice of the cutoff value would be

Table 2. Lennard-Jones Potential Parameters for C-C, C-N$_2$, and N$_2$-N$_2$ Interactions Used in the Molecular Dynamics Generation of [TARGET] and for the Simulated Isotherm Calculations

	σ (Å)	ϵ/k_B (K)
C−C	3.40	28.0
C−N$_2$	3.36	61.4
N$_2$−N$_2$	3.75	95.2
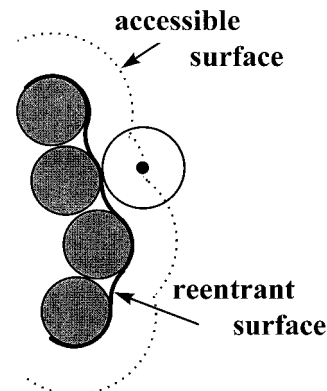
Figure 6. Schematic depicting the definitions of the accessible and the reentrant surfaces.

σ_{NC}, the carbon−N$_2$ interaction diameter. The porosity would then be the fraction of acceptable insertions in the Monte Carlo fashion of integration. However in microporous materials such a measure results in discrepancies when comparing to bulk adsorbate densities. Consider a slit pore in which exactly one monolayer can fit (i.e., each adsorbed nitrogen molecule is in contact with carbon atoms from both layers of the slit pore). In this case, our method would fail to count the volume associated with this monolayer. The reason is that insertions into this narrow pore occur with a vanishing probability in our simple Monte Carlo integration scheme. We therefore make the distinction between *accessible surface* and *reentrant surface*[44,45] (or *Connolly surface*).

Following Gelb and Gubbins,[43] we define the two surface types in Figure 6. The *accessible surface* is defined as the locus of points whos minimum distance to any carbon atom is exactly equal to σ_{NC}. For the *reentrant surface* this distance equals $\sigma_{NC} - 0.5\sigma_{NN}$. Both surfaces can be visualized by tracing an adsorbate molecule along the carbon surface. The center of the adsorbate traces the *accessible surface* while the edge traces the *reentrant surface*. In defining porosity, we must use the *reentrant surface* definition. The porosity is then defined as the fraction of successful insertions based on the *reentrant surface* cutoff distance. In other words, insertions are accepted if the closest distance to any carbon is greater than $\sigma_{NC} - 0.5\sigma_{NN}$.

Table 1 shows a comparison of the porosities between the [TARGET] structure and the [MODEL] structure. Here we again see good agreement with only a 2% deviation. Note that the porosities measured here correspond to a locally averaged porosity, rather than the average porosity of a macroscopic sample of carbon. The pores sizes observed in our samples (see section 4.3) are typically regarded as microporous. However, bulk carbon samples contain regions of large open volumes where the local porosity approaches unity. Due to limitations in the size of our

(43) Gelb, L. D.; Gubbins, K. E. *Langmuir* **1998**, *14*, 2097.
(44) Suzuki, T.; Kaneko, K.; Setoyama, N; Maddox, M.; Gubbins, K. E. *Carbon* **1996**, *34*, 909.
(45) Underwood, E. E. *Quantitative Stereology*; Addison-Wesley: Reading, MA, 1970.

simulation cell, we must necessarily restrict the size of pores we can study. In effect, both the simulation cell size and the target density we input into our model dictate the size of the pores we observe. To better see this, note that the local carbon density in microporous regions is much higher than the average bulk density of a macroscopic sample. In larger simulation cells, we could systematically introduce larger pore regions by reducing the target density. The radial distribution function would still produce an accurate representation of the micropore structure; however, we can arbitrarily introduce larger pore regions represented as void space between microporous crystallites. The fact that we can arbitrarily choose a target density is a result of the wide range of observed *local* carbon density within a macroscopic sample, compared to the relatively small scale of our simulation.

4.2. Surface Area. In carbon structures one is typically interested in measuring the specific surface area (surface area per unit volume). Surface areas are normally measured by fitting nitrogen isotherm data to some prescribed adsorption model—such as the BET or Langmuir isotherms. These models make certain assumptions about how many adsorbate layers form and how adsorbed molecules self-interact.

With our model, we can determine surface area based solely on geometric considerations. We use the *accessible surface* definition described above since it gives a more accurate picture of how surface areas are experimentally measured. The procedure involves randomly choosing a carbon atom and placing a test nitrogen molecule at a distance of σ_{NC} away in some randomly determined direction. The possible positions of the test molecules are then the union of spherical shells centered around all of the carbon atoms. The *specific atomic area* of this surface, as we define it, is $4\rho\sigma_{NC}^2$. An insertion is excepted so long as the minimum distance to any neighboring carbon atom is greater than σ_{NC}. The specific surface area is determined as the fraction of accepted insertions times the *specific atomic area*.

In Table 1 we compare the specific surface areas for the [TARGET] structure and the [MODEL] structure. We see that the [MODEL] structure has a higher surface area by almost 12%. As one would expect, it appears that surface area is more sensitive to the carbon configuration than porosity. We do see that the higher porosity structure also has higher surface area. Again this is to be expected. Some care should be taken in comparing our geometrical surface areas to experimental values. First, our areas do not take into account exclusion of one monolayer by neighboring layers. For instance, if a slit pore were such that only one monolayer could fill it, our method would count this area twice. Second, we are calculating areas based on Monte Carlo principles. Thus we do not take into account accessibility of pores. It is quite possible that certain pore regions that could not be reached though normal molecular motion exist and are erroneously counted in our method.

4.3. Pore Size Distribution. From our model structures we can calculate a pore size distribution based purely on geometry. The procedure is similar to that used by Gelb and Gubbins for CPGs.[46] We define the pore size distribution function $f(H)$ as the fraction of volume corresponding to pore dimension H. We can construct such a function by taking the derivative of a cumulative volume fraction as follows. We define $v(H)$ as the total volume (simulation cell) for which a test sphere of diameter H *or smaller*, whose boundary does not overlap the carbon lattice, can

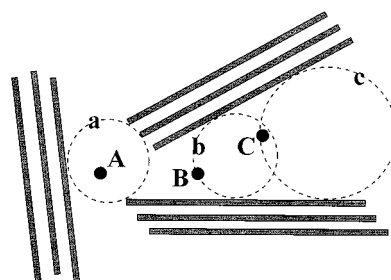(46) Gelb, L. D.; Gubbins, K. E. *Langmuir* **1998**, *15*, 305.

Figure 7. Schematic depiction of computing the pore size distribution in carbon structures. The solid circles labeled A, B, and C represent insertion points, and the dotted circles labeled a, b, and c represent the largest circles one can impose into the structure while still enclosing points A, B, and C, respectively. See section 4.3.
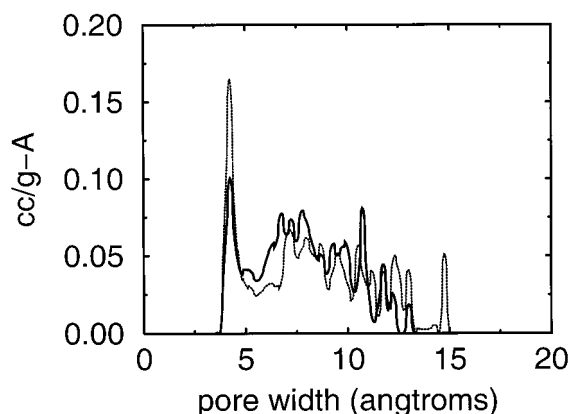

Figure 8. Pore size distributions of the [TARGET] structure (solid line) and the converged [MODEL] structure (dotted line). Units are in cubic centimeters of micropore volume per gram of carbon per angstrom.

enclose. In other words, at each point in our simulation cell, we determine the largest diameter sphere that we can fit into the lattice and still encompass that point. Figure 7 shows a two-dimensional analogue. Spheres a, b, and c correspond to volume points A, B, and C. We construct $v(H)$ as a histogram by counting the number of points for which the corresponding sphere diameter is less than or equal to H. The pore size distribution function is then just the derivative

$$f(H) = -\frac{1}{v_{cell}}\frac{dv(H)}{dH} \tag{5}$$

where v_{cell} is the total volume of the simulation cell.

In Figure 8 we compare the pore size distribution functions for the [TARGET] carbon and the [MODEL] carbon. We note that the qualitative features of the distributions are the same. Both carbons have a peak at around 4 Å corresponding to interlayer separations within crystallites. However, differences in peak shapes and amplitudes are evident. For example, the [MODEL] carbon has a smaller population of 5−7 Å pores yet a larger population of 12+ Å pores. Furthermore, there is a significant peak at around 14.5 Å corresponding to a single "bubble" of void space. Considering the relatively small simulation cell used, the similarities in the pore size distributions are remarkable. It is expected that as the size of the simulation cell is increased, these difference should become less pronounced.

4.4. Surface-Averaged Energy Distribution. One defect of the slit-pore model is its lack of surface energy heterogeneity. In a perfect single slit-pore, molecules
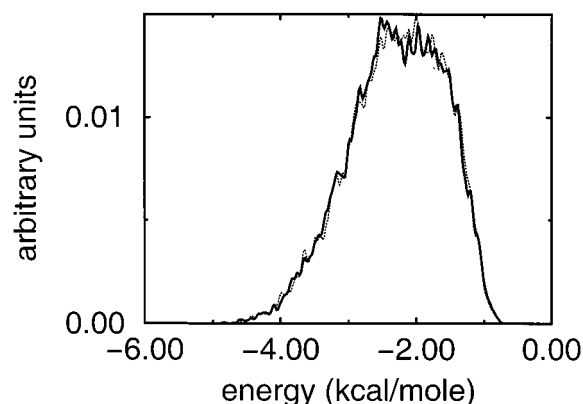
Figure 9. Surface-averaged energy distribution for a spherical Lennard-Jones nitrogen molecule in the [TARGET] structure (solid line) and the [MODEL] structure (dotted line).

Figure 10. Simulated nitrogen adsorption isotherm for the converged [MODEL] structure. Units are in cubic centimeters of nitrogen at STP per gram of carbon.

adsorbed at the surface would be subject to a surface–adsorbate interaction energy that is nearly monodisperse and dependent only on the model pore width. Some dispersion in energy would be observed due to the molecular structure of the carbon surface and would be seen as corrugations on the surface—i.e., valleys and hills corresponding to adsorption at the center of an aromatic ring versus adsorption directly on top of a carbon atom.[42] In real carbons, there is much more structural disorganization leading to more surface energy heterogeneity. A wider distribution in surface energy could, for example, be introduced by (1) noninfinite crystallite sizes, (2) nonparallel carbon plate layering, (3) differences in the number and spacing of stacked layers in a pore wall, (4) a distribution of pore sizes corresponding to distinct surface adsorption energies, and (5) adsorption sites located along crystallite edges.

We can measure heterogeneity in our carbon model by calculating the *surface averaged energy distribution*. We accomplish this in exactly the same manner as for surface area; however, for each successful insertion, we now determine the interaction energy of the adsorbate with the carbon lattice. We then construct an energy histogram from which the distribution can be calculated.

In Figure 9 we show a comparison of surface-averaged energy distributions for both the [TARGET] structure and the [MODEL] structure. In these calculations we again used the Lennard-Jones potential for the spherical nitrogen model with the parameter values found in Table 2. The functions shown in Figure 9 represent the distribution of adsorption site energies the adsorbates would see in the zero density (and pressure) limit—where adsorbate–adsorbate interactions are negligible. They are a measure of the heterogeneity in the surface adsorption energy that arises *purely from the carbon morphology*. Surface energy heterogeneity can also result from difference in site energies, e.g., by including active sites on the carbon plate edges or surfaces due to heteroatoms. We therefore distinguish between these two sources of heterogeneity as *structural heterogeneity* and *chemical heterogeneity*. We see that the two carbon structures in Figure 9 exhibit nearly identical surface-averaged energy distributions and therefore represent the same degree of structural heterogeneity.

5. GCMC Simulations and Adsorption Isotherms

We conducted grand canonical Monte Carlo (GCMC) simulations to calculate the nitrogen adsorption isotherm for our [MODEL] carbon. Nitrogen was modeled using the spherical Lennard-Jones potential. The GCMC method
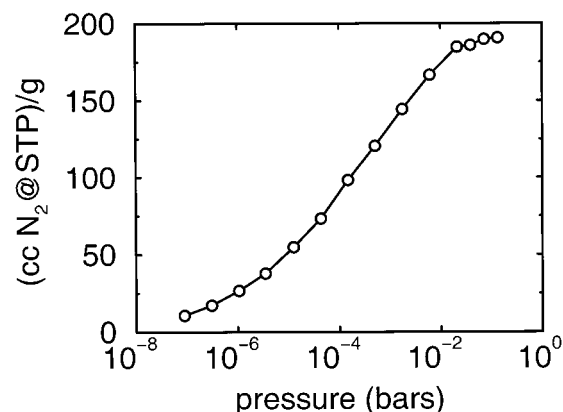
is well-known and used extensively to simulate systems at constant temperature, volume, and chemical potential. The details of this simulation technique can be found in various sources.[39,47–49]

The adsorption isotherm was calculated by conducting GCMC runs at 77 K at incremental values of chemical potential. At least 2 million moves were allowed for equilibration which was monitored closely for each isotherm point. Subsequently, a further 2 million moves were used for data collection and averaging. The move types were distributed with equal probability between insertion/deletion and translation, and the maximum nitrogen displacement was adjusted during equilibration to give a 50% acceptance ratio. Block averages were constructed to estimate the statistical error in averaged values. The values of the Lennard-Jones parameters are given in Table 2.

Chemical potential was adjusted to give a range of bulk pressures up to at least 0.133 bar ($P/P_0 = 0.132$). We related chemical potential in our simulations to absolute pressure in the bulk phase by using a virial expansion truncated at the second virial term. For the Lennard-Jones potential with the nitrogen parameters we used, the second virial coefficient was $B = -210.36$ molecules/cm³ at 77 K. At each isotherm point we measured the average number of adsorbed nitrogen molecules and converted it to units of cm³ (at STP)/(g of carbon). All pressures were reported in bar.

In Figure 10 we show the nitrogen isotherm for the [MODEL] structure up to 0.133 bar. The isotherm is characteristic of a micropore structure, with almost complete nitrogen uptake occurring by $P/P_0 = 0.1$. The shape of the low-pressure part of the isotherm is consistent with a continuous filling description. This was to be expected since the majority of the pore space had pore widths between 7 and 13 Å. However there appears to be a cusp near 0.04 bar that would seem to indicate hysteresis—and would be evidence of capillary condensation. We recall that this particular structure had a single pore with dimensions around 14.5 Å. It is quite possible that condensation occurred within this localized region near the higher end of the pressure scale. Since the contribution to the total pore volume from this "bubble" is relatively small, it would be difficult to detect condensation from the isotherm data.

(47) Allen, M. P.; Tildesley, D. J. *Computer Simulation of Liquids*; Clarendon Press: Oxford, 1987.
(48) Adams, D. J. *Mol. Phys.* **1975**, *29*, 307.
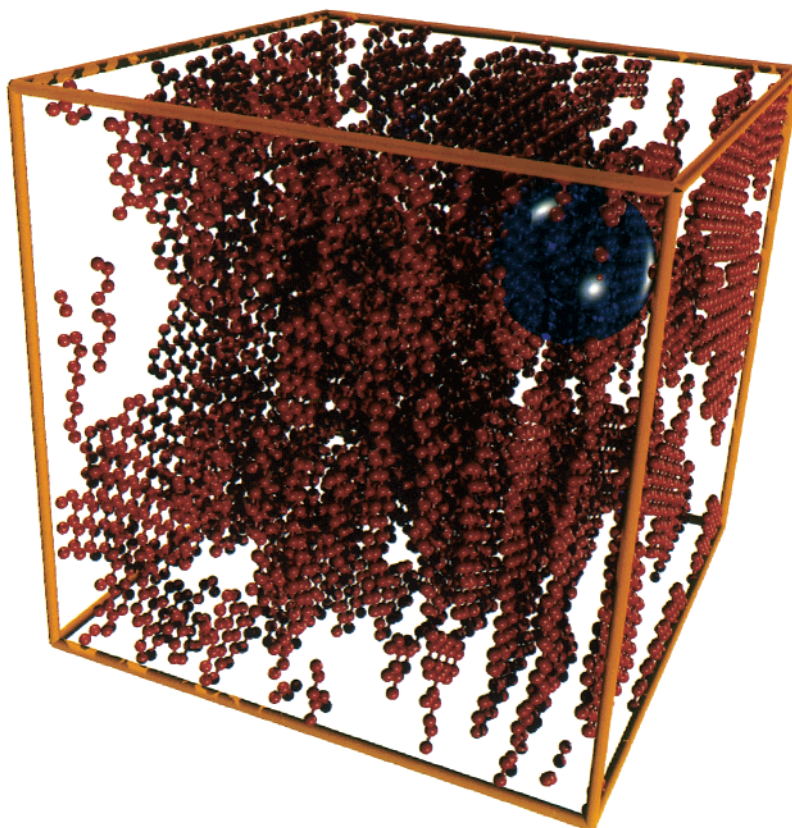(49) Cracknell, R. F.; Nicholson, D.; Quirke, N. *Mol. Phys.* **1993**, *80*, 885.

Figure 11. Structural representation of the converged [MODEL] structure showing the position of the large 14.5 Å pore region (encloded in the blue sphere).

Interestingly, the slit-pore representation is unlikely to provide a good description of the effects of localized condensation for this model carbon. We can see the reason for this in Figure 11, which shows the location of the 14.5 Å pore in the [MODEL] structure. Clearly the pore boundary is non-slit-like and the pore morphology is three-dimensional. Consequently we would not expect the slit-pore model to provide an accurate description of condensation in these situations. This would be true of any carbon in which the local structure resulted in pockets or "bubbles" of mesoporous void space.

The same can be said about the entire scale of pore sizes. The predominant morphology of even the smaller micropores are non-slit-like. In Figure 12 we show snapshots of our GCMC simulation at $P = 0.02$ bar. In Figure 12A we can see the alignment of carbon plates to form crystallites within which nitrogen is excluded. Adsorption occurs between crystallite surfaces in pores that only locally resemble slit-pores. Further, the disorganized arrangement of carbon plates provides a high degree of connectivity between pores. This arrangement results in a highly connected network of pores in which carbon plate edge effects seem to predominate.

6. Experimental Carbon

We next used our RMC procedure to study the structural morphology of an experimental carbon. We used an activated mesocarbon microbead (a-MCMB) sample with an experimental RDF and nitrogen isotherm provided by Katsumi Kaneko and his research group.[50] The a-MCMB sample was obtained from Osaka Gas Co. and activated with KOH. Activated carbon microbeads can be thought of as roughly spherical beads of nanoporous, polycyclic carbon arranged in a randomly packed configuration.

Mesocarbon microbead materials are expected to be more ordered in structure than granular activated carbons (GAC) and activated carbon fibers (ACF) and are thus well suited for our RMC model.[51–53]

We conducted our RMC procedure in a cubic simulation cell which measured 100 Å on a side. A target density of 0.97 g/cm³ was used based on an estimate of the actual carbon density. The true *local* density of carbon micropore regions is experimentally difficult to determine. Therefore we had to rely on an estimate obtained from the experimental radial distribution function. During our RMC simulation, we allowed the model carbon density to deviate through addition and removal of carbon during ring creation/annihilation steps. This in effect allowed the experimental radial distribution function to determine the final output density. Plate creation/annihilation steps were still included; however, a greater tolerance of ±10% deviation in density was imposed (see section 2).

We started with an initial carbon configuration having a mean carbon plate size of $\bar{n}_p \sim 13$ rings/plate. Since we did not have at our disposal any quantitative information on the experimental size distribution of plates, we generated a broad distribution of sizes for our initial structure (ranging from 7 to 44 rings/plate). The plates were randomly placed and oriented in the simulation cell as described in section 2. Approximately 360 000 RMC moves were conducted, after which the square deviation was determined to be converged.

Experimental RDFs are reported in the form $4\pi r^2 \rho(g(r) - 1)$ obtained directly from the transformation of the structure factor (eq 2). Thus, the average *local* density

(50) Kaneko, K., Chiba University, personal correspondence.

(51) Oberlin, A. *Carbon* **1984**, *22*, 521.
(52) Ishii, C.; Matsumura Y.; Kaneko, K. *J. Phys. Chem.* **1995**, *99*, 5743.
(53) Ishii, C.; Shindo N.; Kaneko, K. *Chem. Phys. Lett.* **1995**, *242*, 196.
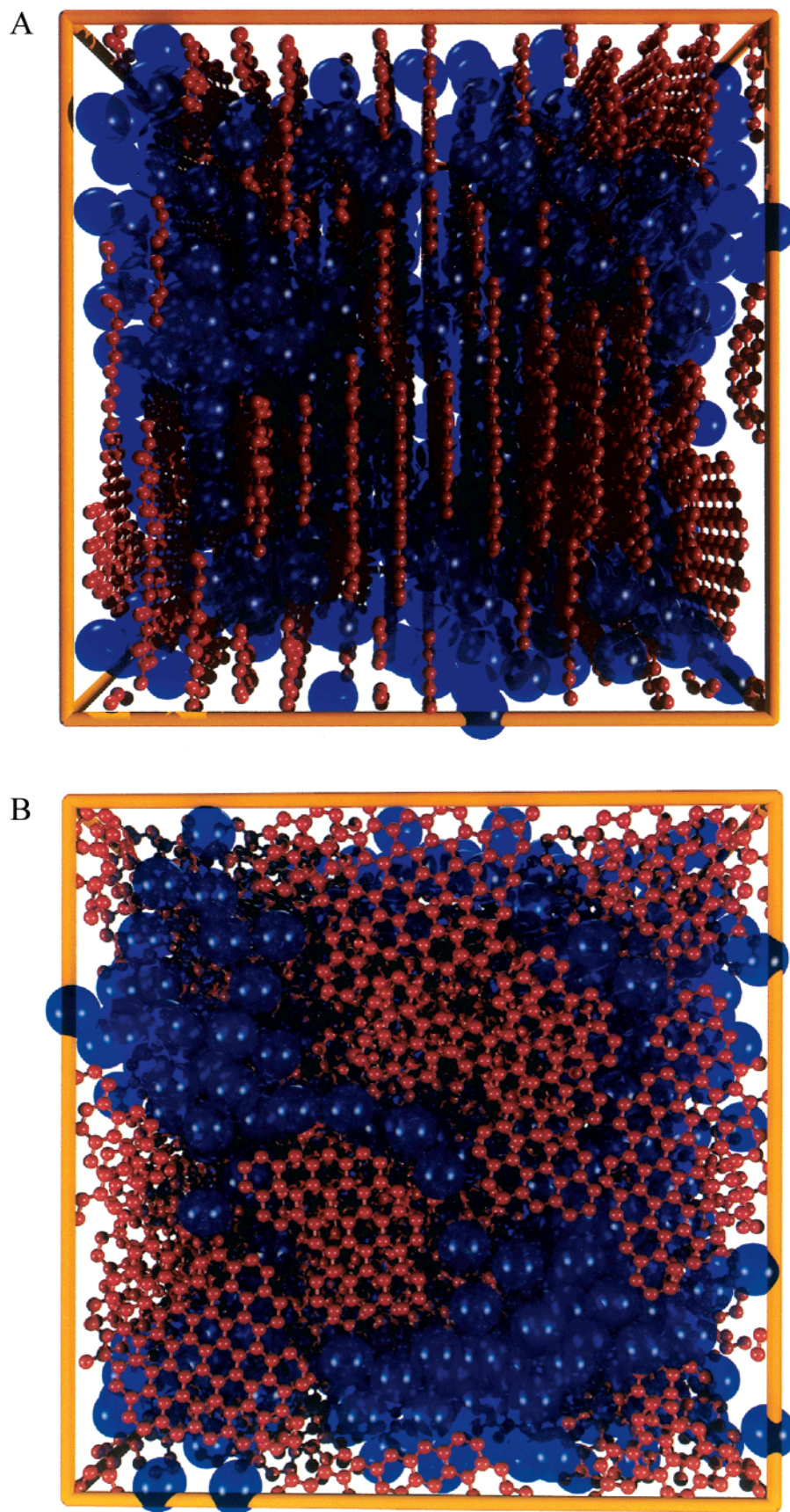
Figure 12. Snapshots from a GCMC simulation of nitrogen adsorption in the converged [MODEL] structure: (A, top) edge view of the carbon structure; (B, bottom) plane-normal view of the carbon structure.

of carbon ρ is not experimentally given. However, calculation of the simulated RDF, in this form, is a simple matter as the simulated carbon density is always known. The degree of Gaussian broadening for the *intraplate* contri-
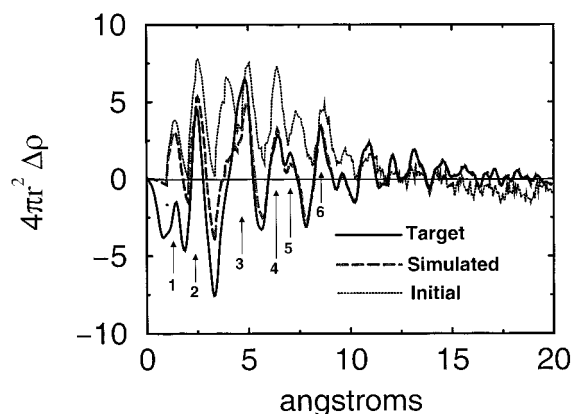
Figure 13. C−C radial distribution functions for the [a-MCMB] structure. The experimental RDF (solid line), the simulated, converged RDF (long-dashed line), and the initial simulated RDF (dotted line) are shown with identified peaks referenced in the text (see section 6).

bution was fixed to match experimental peak widths for the first several peaks of the RDFs (see section 2). Figure 13 contains a comparison of the target (experimental) RDF and the converged (simulated) RDF. Our *initial* simulated RDF is also shown. Beyond a distance of 7 Å the simulated RDF matches exactly with that obtained in the experiment. However, below ∼5 Å the simulated $g(r)$ shows less agreement. We attribute this difference in part to experimental SAXS inaccuracies in small r (large k) resolution of the structure factor. The first peak (labeled 1) shows the largest deviation. The location of this peak represents the direct intraplate C−C distance along sp^2 bonds. However the experimental value of this peak is much too low for the density of carbon considered here. The peaks labeled 2 and 3 show much better agreement.

Peaks 2 and 3 contain contributions from the intraplate structure corresponding to C−C distances both within the same aromatic ring and in neighboring rings. These features are identical to small r X-ray scattering peaks in graphite. In addition, peak 3 contains a large contribution due to *interplate* separations between neighboring plates aligned roughly in parallel. This third peak location (between 4 and 5 Å) therefore identifies the interplate separation distance within carbon plate crystallites. An interesting feature of our simulated RDFs is the reduction of peaks 1−3 from the initial distribution to the final converged RDF. Also the peak initially at 3.85 Å is virtually nonexistent in the converged RDF. The overall reduction in peak sizes is due to a reduction of the carbon plate sizes over the course of the RMC simulation. The converged average plate size was 11.6 rings/plate compared to the initial value of 13. In addition, the peak at 3.85 Å includes contributions from interplate separations and thus merges into peak 3 over the course of the run.

We observe that the RDF for values less than ∼5 Å corresponds exclusively to intraplate contributions. These peaks are refined in our method through ring creation/annihilation and plate creation/annihilation moves. Further, the RDF contributions above 10 Å are mostly due to the relative orientation of the plates and are refined primarily through plate displacement and reorientation moves. We find the RDF above 10 Å converges rapidly whereas convergence of the RDF below 5 Å proceeds slowly. Thus as the simulation begins, we obtain a very rapid optimization of relative carbon plate orientations followed by a long optimization of the size, shape, and number of carbon plates. As the structural characteristics of the plates are slowly adjusted, the relative plate orientations

are continually and rapidly reoptimized. This presents a very efficient algorithm for optimizing carbon structures.

Figure 14 shows the converged structural configuration of our model. The structure contains irregular carbon plates arranged in a layered pattern. Again we observe a pore morphology that is non-slit-like with carbon atoms on the plate edges having a significant contribution to the pore morphology. Unlike our hypothetical carbon structures ([TARGET] and [MODEL]), it is much more difficult to identify definite crystallites of plate groups in the [a-MCMB] structure. In this respect, the carbon structure appears to be more homogeneous, with a fine highly connected pore topology. This type of plate arrangement—along with a highly porous microvolume—is most likely what gives rise to the exceptionally high surface areas observed in a-MCMBs. Table 3 contains the structural characterization of this model carbon including our calculated microporous surface area of 1070 m²/g—compared to a measured total BET surface area of 2200 m²/g. One reason that our surface area is lower than that obtained in the experiment is that we are only modeling the micropore volume and are hence neglecting the appreciable surface area of the mesoporous region. Thus, the experimental value excluding mesopores would be somewhat lower than 2200 m²/g. Despite this fact, it seems that our calculated microporous surface area is significantly lower than that obtained in the experiment. As we will see below, this is in large part due to the inaccuracy of the BET surface area for small pores.

The radial distribution function can be used to obtain qualitative information about the pore size distribution (PSD). In Figure 15 we show the pore size distribution calculated for [a-MCMB] using the method described in section 4.3. We note that the first peak in pore size at 4.5 Å in Figure 15 coincides with peak 3 of the RDF. This corresponds to the nearest neighbor interplate distance. These pores are too small for nitrogen to adsorb into and represent instead near-graphite-like stacking of plates. The next two peaks at 7 and 8.2 Å coincide with peaks 5 and 6 of the RDF. Peak 6 is due primarily to second nearest neighbor interplate distances. The corresponding peak in the (PSD) therefore represents pore regions between two plates separated by a third plate. These pore regions occur from the disordered stacking of carbon plates. We can picture the pore region by imagining two outer plates extending beyond the end of a middle plate. Close examination of Figure 14 shows that such pore configurations occur all throughout the carbon structure, and—as seen in the PSD—they represent the predominant pore size contribution.

We used our output model [a-MCMB] to calculate the nitrogen adsorption isotherm at 77 K using the grand canonical Monte Carlo technique previously described in section 5. Due to the larger simulation cell (100 Å versus 50 Å), we implemented a parallel, domain decomposition GCMC algorithm optimized for 27 processors.[54,55] The calculations were conducted on a Cray T3E distributed-memory supercomputer. Over 100 million moves were required for equilibration and 50 million moves were used for data collection at each isotherm point.

In Figure 16 we show the simulated nitrogen adsorption isotherm compared to experimental values. The isotherm is measured in units of milligrams of adsorbed nitrogen per gram of carbon. The experimental points were obtained by Kaneko and co-workers using the usual gravimetric

(54) Jones, D. M.; Goodfellow, J. M. *J. Comput. Chem.* **1992**, *14*, 127.
(55) Heffelfinger, G. S.; Lewitt, M. E. *J. Comput. Chem.* **1995**, *17*, 250.
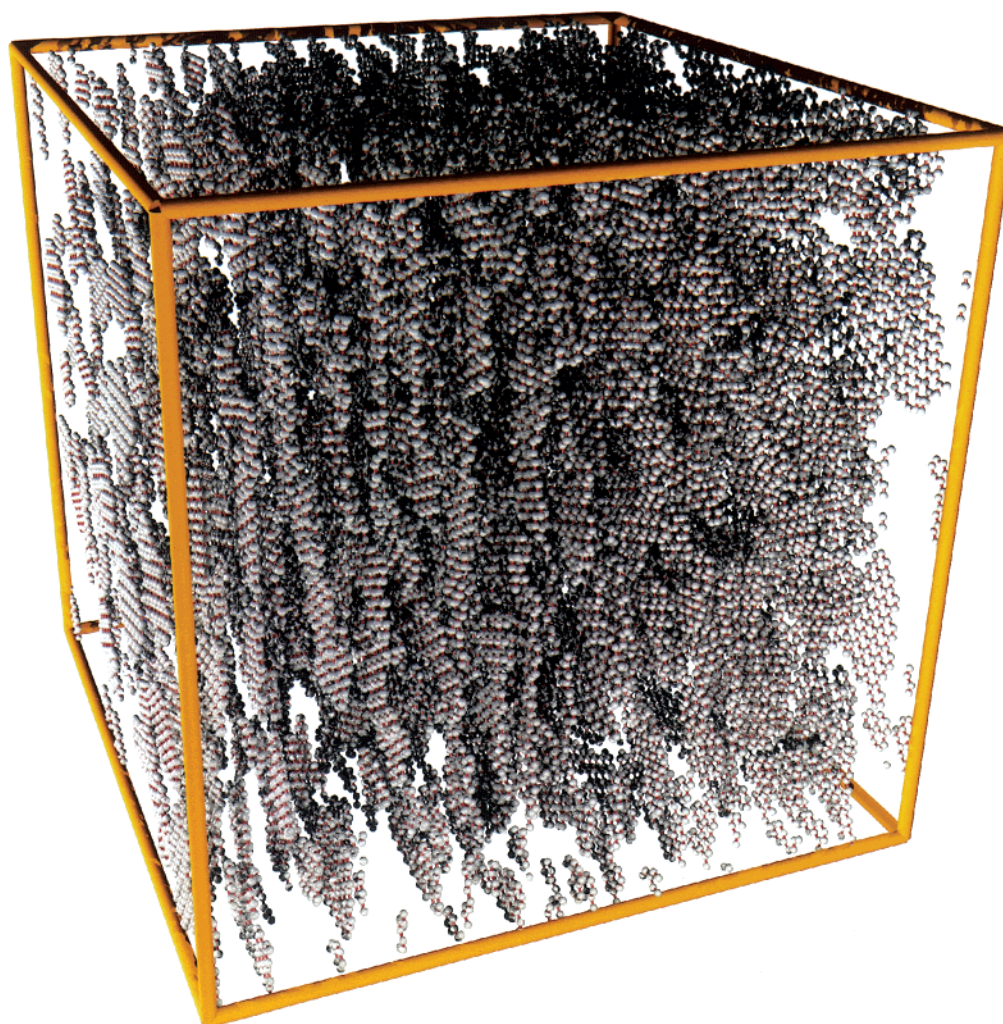
Figure 14. Structural representation of the converged RMC [a-MCMB] structure. Red spheres represent carbon atoms which are shown at a scale much less than their van der Waals radii for reasons of clarity.

Table 3. Calculated Structural Properties of the Converged RMC [a-MCMB] Structure

	[a-MCMB]		[a-MCMB]
density, g/cm^3	0.973	porosity	0.579
n_r (rings/plate)	11.60	surface area, m^2/g	1070
σ_r (std dev)	7.91	BET (simulated), m^2/g	1510
carbons/plate	38.01	BET (exptl), m^2/g	2200

methods at 77 K. We see that up to $P/P_o \sim 10^{-3.3}$, where the experimental measurements begin, the simulated isotherm coincides with the experimental isotherm—connecting up with the experimental curve precisely. Above $10^{-3.3}$ the simulated isotherm starts to plateau somewhere below the experimental curve. We obtain good agreement with the experimental isotherm at the low pressure end—where we expect that micropore filling predominates. However, the fact that the model isotherm exhibits lower nitrogen capacity at higher pressures, and that the model surface area was significantly lower than that obtained in the experiment, shows that we have not obtained an accurate representation of the larger pore size structure.

It is well-known that the BET model[56] overestimates the surface area of small pores—the smaller the pore, the greater the descrepancy. To test this, we used our nitrogen

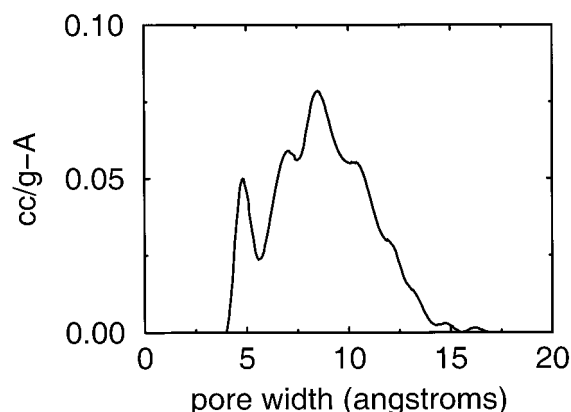(56) Brunauer, S.; Emmett, P. H.; Teller, E. *J. Am. Chem. Soc.* **1938**, *60*, 309.

Figure 15. Pore size distribution of the converged RMC [a-MCMB] structure. Units are in cubic centimeters of micropore volume per gram of carbon per angstrom.

isotherm data to calculate a *simulated BET surface area* based on the equation

$$\frac{P/P_o}{N(1 - P/P_o)} = \frac{1}{cN_m} + \frac{c-1}{cN_m}(P/P_o) \tag{6}$$

Here N_m is the molecular density of an adsorbed monolayer, N is the amount of nitrogen adsorbed at pressure
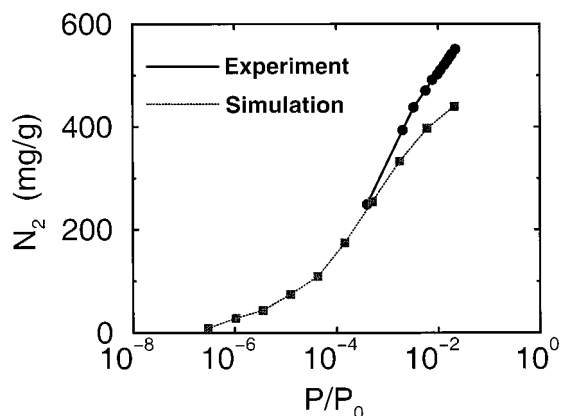
Figure 16. Nitrogen adsorption isotherms for the converged RMC [a-MCMB] structure (dotted line and squares) and experimental data (solid line and circles). Units are in milligrams of nitrogen per gram of carbon.

P, and c is an energy term related to the net heat of adsorption. Using a monolayer surface density of 16.2 Å^2 per nitrogen molecule, we calculated the BET surface area by linear regression of the isotherm fitted to eq 6. The surface areas are compared in Table 3. Our simulated BET surface area of 1510 m^2/g is approximatedly 41% higher than the surface area calculated from the RMC model structure (1070 m^2/g). This clearly shows that the BET surface area is an inaccurate characterization of a microporous surface. Although the BET method is successful for quantifying large mesoporous surface areas, great care should be taken in using BET measurements of surface area as parameters in thermodynamic adsorption models where mircopore contributions are significant.

7. Discussion and Conclusions

In this study we have developed a method for obtaining structural carbon models that more accurately represent the true carbon and pore morphology of porous carbons. We have shown that the RMC method is a viable method for optimizing simulated C–C radial distribution functions relative to experimental inputs. Consequently, the RMC method allows one to generate structural models based on true structural input obtained experimentally. Our method is not limited to carbon pair correlation functions. In fact any experimental input data that can be simulated structurally (i.e., that is a function of the carbon atom positions) could be included in this method.

Once a model has been generated, it is possible to analyze structural properties of the micropore morphology. We have calculated quantities, such as the porosity and surface area, and have obtained pore size distributions dependent solely on the carbon structure. We have also developed methods for determining the surface-averaged adsorption energy and have simulated, through GCMC methods, the nitrogen adsorption isotherms. These are potentially valuable tools for analyzing the pore structure of porous carbons. In addition, the results for the model carbons can be used to test the accuracy of classical methods for characterizing microporous carbons. For example, the simulated nitrogen adsorption isotherms for a model carbon can be used to estimate BET surface area,[43] pore size distribution (PSD) by the BJH,[46] DFT, or other

methods, etc. Such approximate estimates can be compared to the exactly known surface area and PSD—determined from the model—and can provide an unambiguous way to test these widely used classical methods.

Although our model provides a reasonable representation of the micropore structure, we have encountered difficulties in representing the larger pore size regions. In addition, we have not yet been able to generate mesopores. This is presumably due to the nonuniqueness of the RDF optimization as well as to the weak sensitivity of $g(r)$ to long-range correlations. A mesopore represents a large void region in the structure. This corresponds merely to reductions in the RDF peaks at values less than the mesopore diameters. Thus there is no real direct means of incorporating mesoporous structure using simply the C–C radial distribution function. Consequently there is no direct means of specifying the existence of mesoporous regions in our model. Rather, the RMC method establishes a nonunique representation of the experimental RDF that does not necessarily include mesopores. One way to get around this problem would be to include correlation functions that are specifically sensitive to long-range mesopore structure. For example, one could extract pore–pore correlation functions directly from TEM micrographs of porous carbons and use these as targets in the RMC procedure. We plan such a study soon.

The model we presented here used a simplified representation of aromatic carbon plates; i.e., we assumed a planar configuration of polyaromatic carbon sheets. In actual porous carbons, the carbon plates often contain defects in the form of nonaromatic 5-, 6-, and 7-fold ring units. These defects result in nonplanar configurations of plates that are curved and twisted. There is also usually a significant quantity of heteroatoms such as oxygen, hydrogen, and sulfur that can add to the structural heterogeneity by bonding directly to the carbon plates. This can produce more complex bonding structures within the plates, as well as allowing cross-linking of plates though bridging bonds. We expect these factors to have significant effects on the pore morphology of some highly activated carbons, and future efforts will include refinement of our model to incorporate these effects. At the same time, as more complicated carbon models evolve, it becomes necessary to improve upon the interaction potentials of these structures with adsorbates. For instance, in our adsorption work we assumed a single pairwise interaction potential between carbon and nitrogen irrespective of the carbon's position within a given plate. In actuality we expect carbons along the edge of our plates to be chemically different than interior carbons. Also, we have not yet considered the effect of chemically active sites along the boundary of our plates—an important factor in directing adsorption characteristics of weakly adsorbing molecules such as water.